applied sciences

MDPI

Article

Design of Multi-Wing Deployment Mechanism Based on Multiple Performance Indicators and Topology: Theoretical and Experimental Study

Guangqing Zhai, Jianguo Tao, Hong Xiao *, Hongwei Guo, Guang Yang, Runchao Zhao, Chen Yao and Rongqiang Liu

State Key Laboratory of Robotics and Systems, Harbin Institute of Technology, Harbin 150006, China; 20b908100@stu.hit.edu.cn (G.Z.); jgtao@hit.edu.cn (J.T.); guohw@hit.edu.cn (H.G.); yangguang346@126.com (G.Y.); zhaorc@hit.edu.cn (R.Z.); yaocxx@126.com (C.Y.); liurq@hit.edu.cn (R.L.)

* Correspondence: xiaohong@hit.edu.cn

Abstract: The folding wing deployment mechanisms of aircraft are constrained by weight and space limitations, necessitating fewer actuators, multiple outputs, compact designs, and high efficiency. However, existing folding wing mechanisms often overlook the impact of performance in configuration design. Additionally, they struggle to achieve the synchronous unfolding of multiple wings using a single drive. This paper presents a design methodology for multi-wing deployment mechanisms based on configuration topology and multiple performance indicators. Specifically, seventeen configurations of multi-wing deployment mechanisms are developed based on functional requirements, along with expression methods for performance indicators, including compactness, mechanism stiffness, dynamic sensitivity, motion transmission, and joint transmission efficiency. The optimal configuration for the multi-wing deployment mechanism is identified utilizing the fuzzy comprehensive evaluation. Moreover, the transmission efficiency of multiple configurations is calculated across different scale parameters. Simulation analyses and prototype experiments are conducted to validate the design. The results indicate that the transmission efficiency of the optimized configuration consistently exceeds that of the other configurations. Maximum efficiencies surpass those of the other configurations by 2.4% and 5.7%. Importantly, this study introduces a quantitative expression method for multiple performance indicators at the configuration design stage. This approach enables the integration of various performance metrics with configuration designs. Overall, this research provides a novel approach for the innovative design of multi-wing deployment mechanisms in aircraft. Additionally, considering performance in the selection of mechanism configurations during engineering design offers valuable insights and potential applications.

Keywords: folding wing; configuration synthesis; comprehensive evaluation; mechanism design

Citation: Zhai, G.; Tao, J.; Xiao, H.; Guo, H.; Yang, G.; Zhao, R.; Yao, C.; Liu, R. Design of Multi-Wing Deployment Mechanism Based on Multiple Performance Indicators and Topology: Theoretical and Experimental Study. *Appl. Sci.* **2024**, *14*, 11672. https://doi.org/10.3390/app142411672

Academic Editor: Rosario Pecora

Received: 28 October 2024
Revised: 11 December 2024
Accepted: 12 December 2024
Published: 13 December 2024

1. Introduction

The development trend of various aircraft emphasizes longer range, smaller size, and reduced weight. The constraints of space and weight necessitate a compact design for functional mechanisms. For instance, applying folding wing technology significantly reduces the radial dimensions of aircraft before flight [1,2]. Folding wings typically unfold from a stowed position through the action of deployment mechanisms, providing aerodynamic lift [3–5]. Scholars have made substantial progress in the design of folding wing deployment mechanisms, most of which are planar linkages, such as the link-slider and rocker-slider mechanisms [6,7]. For folding wings used in aircraft, the deployment mechanism must meet technical requirements to automatically unfold to the designated position, fulfilling the specified design criteria of the mechanism. However, as aircraft design diversifies, the demand for folding wing deployment mechanisms is increasing. To minimize the weight of the folding wing deployment mechanism and the number of actuators, it is particularly important to achieve the synchronized deployment of multiple wings using a single actuator within a confined and enclosed space [8]. There is a particular need to achieve synchronous deployment of multiple wings using a single drive within confined spaces. This necessitates the development of new linkage configurations. Moreover, the design process of existing deployment mechanisms fails to account for their impact on performance, leading to systems that, while functional, exhibit suboptimal efficiency. Such challenges hinder the application and advancement of folding wings in aircraft design.

Configuration synthesis is a critical method for studying folding and deployment mechanisms and serves as a key approach to achieving innovative designs for folding wing deployment mechanisms. To achieve innovative designs for folding wing deployment mechanisms, it is essential to select an appropriate link mechanism suitable for such applications. The synthesis and optimization of linkages aim to design a mechanism that meets the intended functional requirements while exhibiting favorable motion and dynamic characteristics [9–11]. Scholars have researched the configuration synthesis of deployable mechanisms [12–16]. For instance, Dobrjanskyj and Freudenstein [17] successfully combined Polya's theory with graphical tools for adding two-joint linkages, synthesizing 16 types of eight-bar, one-degree-of-freedom (1-DOF) motion chains. Additionally, Ding et al. [18] proposed an automated process for synthesizing planar 1-DOF motion chains with varying link types. This research established a database of 1-DOF motion chains with six, eight, ten, twelve, and fourteen links, demonstrating the effectiveness of the method. The above studies on planar mechanism synthesis primarily concentrate on the methods of motion chain synthesis. Nonetheless, they often overlook the subsequent optimization and selection processes.

As research progresses, scholars have made significant theoretical advancements in configuration optimization [19–23]. Yoon et al. [24] proposed a configuration design method that takes constraint forces into account. In this approach, unit masses are assigned to simulate rotational joints drawing on a specified number of degrees of freedom. This approach analyzes the dynamic characteristics resulting from the combination of unit mass and constraint forces. While this method allows for topological optimization of planar rigid-body mechanisms, it focuses solely on the impact of constraint forces, lacking other performance impacts. Liu et al. [25] established a constraint model for motion generation and a dynamic model for four-bar mechanisms, thereby linking the synthesis of linkages with their dynamic performance. This approach allows for the identification of optimal configurations for four-bar mechanisms. It ensures precise motion at the specified task positions and minimizes wear at joint interfaces to enhance durability and efficiency. However, the complexity of the dynamic model, which accounts for joint clearances, limits the applicability of this method to the optimization of mechanisms with a greater number of components. Han et al. [26] introduced an innovative topology optimization method that simultaneously accounts for both kinematic and flexibility characteristics. This approach is tested and validated using a simplified two-dimensional vehicle suspension design. In contrast, most existing linkage mechanisms demonstrate minimal flexibility effects. As a result, treating flexibility as a singular influencing factor restricts its applicability to only specific mechanisms. This limits the broader universality of design approaches. Wang et al. [27] introduced a novel configuration synthesis and selection method for multi-loop serial mechanisms. This approach synthesizes basic closed-loop units utilizing conditions such as the types of fundamental units, contact points, and input–output relationships. By further weighting the adjacency matrix to assess the connectivity of the mechanisms, an entropy weighting method is employed to establish composite evaluation coefficients for assessing the quality of the configurations. While this research emphasizes the innovation of the comprehensive evaluation method, it has yet to establish an intrinsic link between mechanism performance and configuration.

In existing configuration optimization processes, researchers have proposed various methods that enrich the theoretical framework of configuration synthesis for planar linkages. However, relying on a single performance metric as the optimization target lacks a holistic approach. In the design of multi-wing deployable mechanisms, it is essential to consider additional performance indicators specific to unique operating conditions, such as mechanism compactness, configuration stiffness, dynamic sensitivity, motion transferability, and the transmission efficiency of joints. Existing studies rarely incorporate these performance metrics into configuration optimization, leaving a critical gap in the field. This limitation makes it difficult to establish a quantitative relationship between configuration and multiple performance indicators. This limitation hinders a reasonable integration of diverse performance impacts. The demanding operational environment of folding wing deployment mechanisms necessitates stringent design criteria. In this context, the optimization of configurations during the design phase directly influences the characteristics of the mechanisms. Establishing a systematic configuration optimization method can significantly enhance the operational performance of multi-wing deployment mechanisms. This paper proposes a design methodology for multi-wing deployment mechanisms. The approach leverages configuration topology and a comprehensive evaluation of multiple performance indicators. It aims to facilitate the integration of performance with mechanism configurations.

This research offers a novel approach to configuration optimization that considers performance while also achieving innovative designs for multi-wing deployment mechanisms in aircraft. The main contributions and innovations of this study are as follows:

(1) We develop a quantitative expression method for various performance indicators for the design configuration of mechanisms, facilitating the integration of multiple performance metrics with the mechanism configuration.

(2) Through comprehensive evaluation, we identify the optimal configuration for the multi-wing deployment mechanism and conduct simulations and experiments to verify its effectiveness.

The structure of this paper is organized as follows: Section 2 specifies the topological configurations based on the requirements of the multi-wing deployment mechanism, resulting in various configurations of multi-wing deployment mechanisms. Section 3 introduces the performance indicators of the mechanism and presents calculations to obtain the optimal configuration through a comprehensive evaluation. Section 4 calculates the transmission efficiencies of multiple configurations across different scales and conducts simulations and experiments to validate the rationale of the multi-wing deployment mechanism. Finally, Section 5 presents the main conclusions.

2. Configuration Topography

To achieve the functional requirement of synchronous deployment of three folding wings in an aircraft with a single drive, this section conducts similarity identification of the topology graph for eight-bar mechanisms and selects functional points, resulting in seventeen configurations of multi-wing deployment mechanisms.

2.1. Configuration Specific Topology

Due to constraints in spacecraft payload space and weight, the development of multi-wing deployment mechanisms has been significantly advanced. As shown in Figure 1, the folding wings are initially positioned close to the spacecraft. Three sets of folding wings are circumferentially distributed at the top, left, and right positions of the spacecraft. After launch, these three sets of folding wings deploy into place under the actuation of the mechanism. This study focuses on the configuration topology and optimization of a multi-wing deployment mechanism designed to achieve the synchronized deployment of the three sets of folding wings, as illustrated in Figure 1, using a single-drive system.

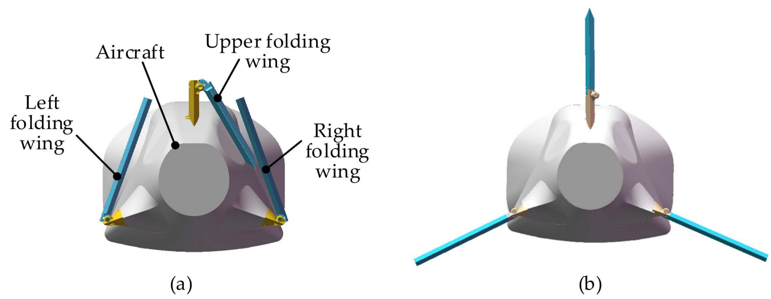

Figure 1. Synchronized deployment requirement of three folding wings: (**a**) initial folded state, (**b**) fully deployed state.

In the configuration synthesis and innovative design of planar mechanisms, the first step is to determine the degrees of freedom, the number of components (the links primarily constitute the main components of planar mechanisms), and the number of joints (joints serve as the movable connections between the components). This determination is contingent upon the input and output requirements of the mechanism. To achieve the synchronous deployment of the three tails, the mechanism must include three rotational joints. Additionally, folding wings require sub-second actuation, which necessitates overcoming aerodynamic loads during the deployment process. The pyrotechnic drive is a commonly used driving method that provides high driving force within a short transient time, and the pyrotechnic drive has a small volume and light weight, meeting the drive source requirements for folding wings. Since the driving source is typically pyrotechnics that generate linear motion, the mechanism should incorporate a translational joint. The transient output force of the pyrotechnic is substantial, necessitating a direct connection to the frame (the frame is the stationary component in a planar linkage mechanism, serving as the main support structure. It is used to support, fix, or connect other parts of the mechanism). Since the three wings rotate around a fixed point on the frame during deployment, the frame should incorporate more than four motion joint connections. The mechanism operates with a single degree of freedom and requires at least four motion joints. To avoid excessive complexity, the fewer the components, the simpler the mechanism while achieving the desired motion. Therefore, the number of active components is set to 7, corresponding to an 8-link and 10-joint single-degree-of-freedom mechanism, for the configuration synthesis of the multi-wing deployment mechanism.

As illustrated in Figure 2, the topology of the seven specific eight-bar, ten-joint configurations that meet these requirements is presented.

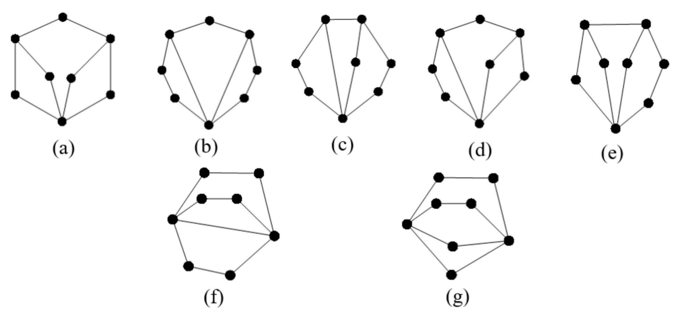

Figure 2. Topography of the particularized eight-bar mechanism: (**a**) Topography a; (**b**) Topography b; (**c**) Topography c; (**d**) Topography d; (**e**) Topography e; (**f**) Topography f; (**g**) Topography g.

2.2. Similarity Point Discrimination

The point degree indicates the number of edges or neighboring vertices connected to it in the topology. As presented in Figure 3, point 1 is a four-degree point, point 2 is a two-degree point, and point 3 is a three-degree point. A path or chain in a topology is an alternating, non-repeating sequence of vertices, and the adjacency matrix expresses the point-to-point connection relationship. The elements of this matrix can be calculated using Equation (1).

$$a_{ij} = \begin{cases} 1 & i \text{ is adjacent to } j \\ 0 & \text{others} \end{cases} \tag{1}$$

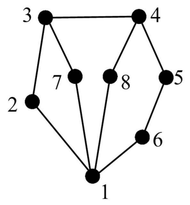

$$\mathbf{A} = \begin{bmatrix} 0 & 1 & 0 & 0 & 0 & 1 & 1 & 1 \\ 1 & 0 & 1 & 0 & 0 & 0 & 0 & 0 \\ 0 & 1 & 0 & 1 & 0 & 0 & 1 & 0 \\ 0 & 0 & 1 & 0 & 1 & 0 & 0 & 0 \\ 0 & 0 & 0 & 1 & 0 & 1 & 0 & 0 \\ 1 & 0 & 0 & 0 & 1 & 0 & 0 & 0 \\ 1 & 0 & 1 & 0 & 0 & 0 & 0 & 0 \\ 1 & 0 & 0 & 1 & 0 & 0 & 0 & 0 \end{bmatrix}$$

Figure 3. Topography of an eight-bar mechanism with adjacency matrix.

In Figure 3, the Arabic numerals (1, 2, 3, etc.) represent the point numbers in the configuration topology diagram.

Although the shapes and labeling of topologies differ, their point-edge connection relationships remain identical, often resulting in duplicate functional topologies during function point selection. To address the issue of isomorphism in the synthesis process, similarity point identification is performed using the topological quadruple power matrix and distance matrix eigenmodes. This enables accurate selection of function points by analyzing similarity through multiple matrices.

(1) Weighting matrix. In topology, numerical values can be assigned to lines corresponding to joints to represent their characteristics, known as assignments [28]. These values are applied to the edges of the lines, resulting in a weighting matrix. The elements of this matrix must satisfy the conditions outlined in Equation (2).

$$a_{ij}^{q} = \begin{cases} 1/d & (i \text{ is adjacent to } j) \\ 0 & (i \text{ and } j \text{ are not neighbours}) \end{cases} \tag{2}$$

where d is the largest point degree of the point i, j.

(2) Quadruple power matrix and minimum distance matrix. The weighting matrix is calculated using quadruple power to obtain the weighted quadruple power matrix. Before calculating the minimum distance matrix, the weighting matrix must first be transformed. The Warshall–Floyd algorithm [29] can then be applied to compute the minimum distance matrix from the processed weighting matrix. The details of the algorithm are not introduced in this paper.

The resulting quadruple power matrix and minimum distance matrix are sorted in descending order to produce two types of eigenmodes for each vertex. These eigenmodes represent the fixed position of the vertex within the topology and its connection relationships. If two vertices in the same topology represent the same quadruple power and minimum distance eigenmodes, they are considered similar; otherwise, they are distinct.

Table 1 presents the corresponding quadruple power eigencodes and minimum distance eigencodes for each point in the topology depicted in Figure 3.

Table 1. Eigencodes for each vertex.

Point	A_1^4	M
1	[0.113 0.111 0.095 0.049 0.032 0.014 0.009 0.009]	[0.032 0.027 0.016 0.016 0.014 0.009 0.009 0]
2, 7	[0.086 0.080 0.080 0.064 0.036 0.009 0.007 0.007]	[0.036 0.017 0.014 0.014 0.009 0.004 0.007 0]
3	[0.164 0.111 0.110 0.069 0.014 0.007 0.007 0.007]	[0.038 0.016 0.014 0.014 0.007 0.007 0.007 0]
4	[0.171 0.122 0.086 0.086 0.049 0.024 0.014 0.010]	[0.027 0.024 0.017 0.017 0.017 0.014 0.010 0]
5	[0.171 0.110 0.090 0.072 0.010 0.007 0.007 0.007]	[0.035 0.016 0.014 0.010 0.007 0.007 0.007 0]
6	[0.137 0.120 0.064 0.064 0.038 0.014 0.007 0.007]	[0.038 0.017 0.014 0.014 0.014 0.007 0.007 0]
8	[0.072 0.069 0.067 0.038 0.036 0.036 0.032 0.024]	[0.038 0.038 0.036 0.036 0.035 0.032 0.024 0]

By comparing the feature codes of each vertex, the similar point groups in the configuration topology in Figure 3 are identified as {[1]; [2, 7]; [3]; [4]; [5]; [6]; [8]}. Identifying these similar points is crucial for selecting functional points in the topology. Similarly, Table 2 presents the results of similarity point identification for the seven eight-bar topologies.

Table 2. Judgment of similarity points of the topographies.

No.	Topography	Similarity Point	No.	Topography	Similarity Point
(a)	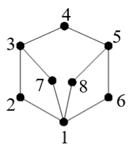	[1]; [2, 6, 7, 8]; [3, 5]; [4]	(b)	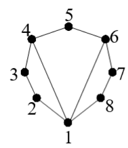	[1]; [2, 8]; [3, 7]; [4, 6]; [5]
(c)	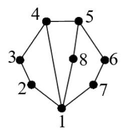	[1]; [2]; [3]; [4]; [5]; [6]; [7]; [8]	(d)	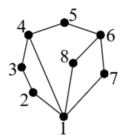	[1]; [2]; [3]; [4]; [5]; [6]; [7]; [8]
(e)	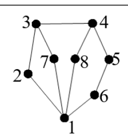	[1]; [2, 7]; [3]; [4]; [5]; [6]; [8]	(f)	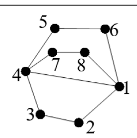	[1, 4]; [2, 3, 5, 6, 7, 8]
(g)	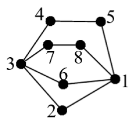	[1, 3]; [2, 6]; [4, 5, 6, 7, 8]			

Note: The topography numbers in Table 2 correspond to the topography numbers in Figure 2.

2.3. Configuration Topography Evolution

The synthesized topology is labeled with function points to generate the mechanism's multicolor topology. The mechanism multicolor topography can indicate the relative positions of the function points, including the rack position points, input position points, and output position points, which are marked with red circles, green triangles, and blue squares, respectively.

Considering that the driver output generates a significant transient output force, it is essential to ensure that one end is directly connected to the frame. The three folding wings unfold to rotate around the frame, which connects to one input point and three output points. Using configuration (a) as an example, the required similarity points of the topology yield two groups of multicolor topographies for the eight-bar mechanism, as illustrated in Figure 4. Similarly, function point synthesis is conducted for several other topologies, with the results summarized in Table 3.

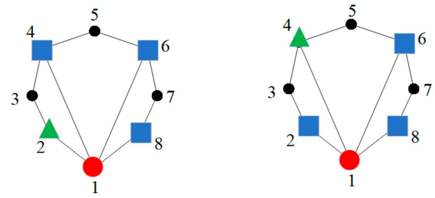

{[1]; [2]; [4, 6, 8]}
(**a**)

{[1]; [4]; [2, 6, 8]}
(**b**)

Figure 4. Multicolor topographies of corresponding function point groups: (**a**) Selection of the first set of functional points; (**b**) Selection of the second set of functional points.

Table 3. Multicolor topographies of the mechanism.

No.	Function Point Synthesis Results	No.	Function Point Synthesis Results
(a)	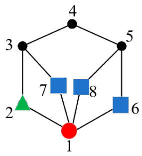	(b)	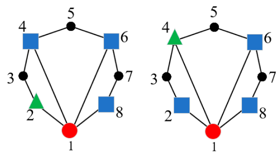
(c)	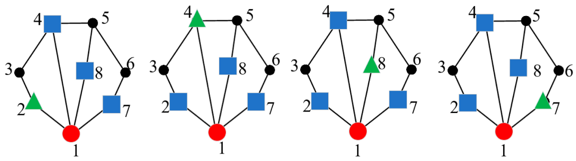		
(d)	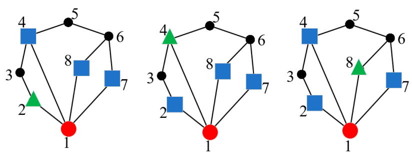	(e)	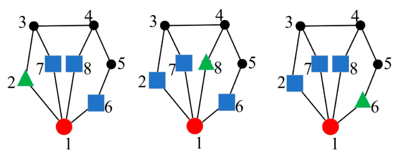
(f)	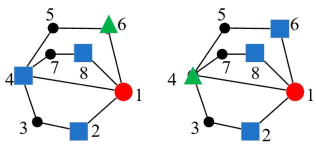	(g)	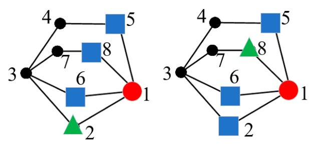

Note: The topography numbers in Table 3 correspond to the topography numbers in Figure 2.

The configuration sketch of the planar mechanism provides an intuitive representation of its appearance and characteristics. Thus, as demonstrated in Figure 5, the configuration sketches of seventeen mechanisms corresponding to the multicolor topology diagrams of multi-wing deployment mechanisms are presented separately.

In Figure 5, configuration (a) corresponds to the topography in Figure 2a; configurations (b) and (c) correspond to Figure 2b; configurations (d), (e), (f), and (g) correspond to Figure 2c; configurations (h), (i), and (j) correspond to Figure 2d; configurations (k), (l), and (m) correspond to Figure 2e; configurations (n) and (o) correspond to Figure 2f; and configurations (p) and (q) correspond to Figure 2g.

In Figure 5, the Arabic numerals (1, 2, 3, etc.) denote the component identifiers of the mechanism.

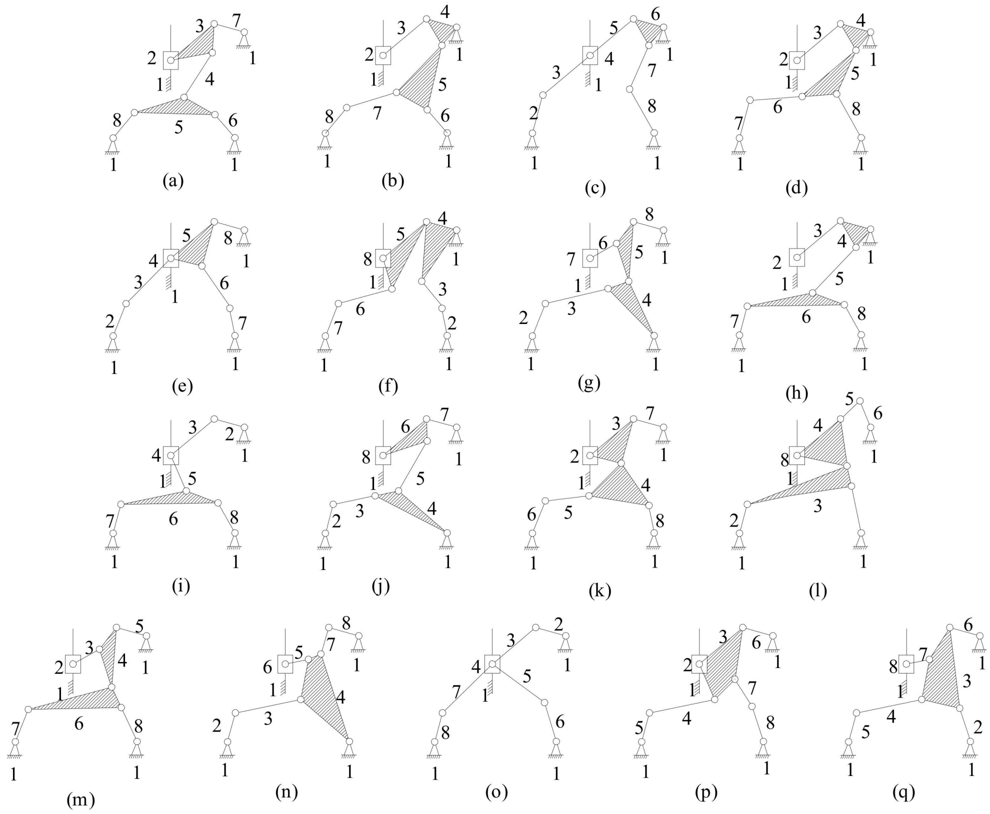

Figure 5. Sketch of seventeen types of multi-wing deployment mechanism configurations: (**a**) configuration a; (**b**) configuration b; (**c**) configuration c; (**d**) configuration d; (**e**) configuration e; (**f**) configuration f; (**g**) configuration g; (**h**) configuration h; (**i**) configuration i; (**j**) configuration j; (**k**) configuration k; (**l**) configuration l; (**m**) configuration m; (**n**) configuration n; (**o**) configuration o; (**p**) configuration p; (**q**) configuration q.

3. Comprehensive Evaluation of Configuration

In the second section, seventeen multi-wing deployment mechanism configurations that meet the design requirements are identified. Taking into account the practical application context and performance criteria of the folding wing mechanism, this section introduces several performance indicators, including structural compactness, stiffness, dynamic sensitivity, motion transmission, and joint transmission efficiency. These performance indicators for the seventeen configurations from Section 2 are quantified, followed by a comprehensive evaluation to select the optimal configuration.

3.1. Mechanism Performance Indicators

The components and joints are numbered for easy analysis, as shown in Figure 6 for mechanism configuration (a).

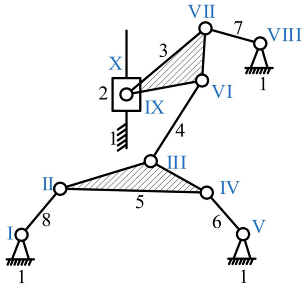

Figure 6. Numbering of components and joints of configuration (a).

In Figure 6, the Roman numerals (I, II, III, etc.) represent the joint identifiers of the mechanism, while the Arabic numerals (1, 2, 3, etc.) denote the component identifiers of the mechanism.

(1) Compactness. In the design of mechanism configurations, the lengths and dimensions of the links (links are primary components of a planar mechanism, serving as a key part of its structure) are not considered. When evaluating the compactness of a link mechanism, a smaller number of links and joints indicates better compactness. If two configurations have the same number of links and joints, compactness is further assessed by determining the minimum number of joints separating two connected links. From the definition of compactness, the space matrix L of mechanism configuration (a) of Figure 6 is obtained.

$$L = \begin{array}{r} \text{Link 1} \\ \text{Link 2} \\ \text{Link 3} \\ \text{Link 4} \\ \text{Link 5} \\ \text{Link 6} \\ \text{Link 7} \\ \text{Link 8} \end{array} \begin{bmatrix} 0 & 1 & 2 & 3 & 2 & 1 & 1 & 1 \\ 1 & 0 & 1 & 2 & 3 & 2 & 2 & 2 \\ 2 & 1 & 0 & 1 & 2 & 3 & 1 & 3 \\ 3 & 2 & 1 & 0 & 1 & 2 & 2 & 2 \\ 2 & 3 & 2 & 1 & 0 & 1 & 3 & 1 \\ 1 & 2 & 3 & 2 & 1 & 0 & 2 & 2 \\ 1 & 2 & 1 & 2 & 3 & 2 & 0 & 2 \\ 1 & 2 & 3 & 2 & 1 & 2 & 2 & 0 \end{bmatrix}$$

The elements of the spatial matrix L represent the minimum number of joints between a selected link and any other link, with diagonal elements being zero. A lower sum of the matrix components indicates a more compact mechanism. Using this method, the compactness values of all the mechanism configurations in Figure 5 are calculated by analogy, with the results presented in Figure 7a.

(2) Stiffness. The actual stiffness of each link in the mechanisms primarily depends on the size, elasticity, and support of the links. For the configurations in Figure 5, the dimensions of the links are not considered. The links are treated as elastic bodies, with the number of joints for each link equal to the number of support points. The stiffness of the mechanism is then represented using the stiffness matrix (Equation (3)).

$$K = \begin{bmatrix} k_1 & k_2 & \cdots & k_i \end{bmatrix} \tag{3}$$

where i denotes the number of independent loops (loops refer to closed kinematic chains in a planar linkage mechanism, consisting of the frame–driving components–driven components–output components and returning to the frame) of the mechanism, and the elements in the matrix can be calculated according to the Equation (4).

$$k_i = \frac{1}{1/c_{i1} + 1/c_{i2} + \ldots + 1/c_{ij}} \tag{4}$$

where c_i, c_j, and c_s are the number of joints from the input to the output component 1, 2, …, j in the independent loop.

As shown in Figure 6, k_1 represents the stiffness value of the loop 2-3-7. Component 2 has two kinematic pairs, component 3 has three kinematic pairs, and component 7 has two kinematic pairs, resulting in $k_i = \frac{1}{1/2+1/3+1/2}$ = 3/4.

The rigidity matrix of the mechanism configuration of Figure 6 can be obtained as $K = \begin{bmatrix} 3/4 & 6/13 & 6/13 \end{bmatrix}$. In the stiffness matrix K, each element is summed to yield the overall stiffness value of the mechanism configuration, with the configuration in Figure 6 having a stiffness value of 1.637. Figure 7b shows the calculated stiffness values for all the mechanism configurations depicted in Figure 5.

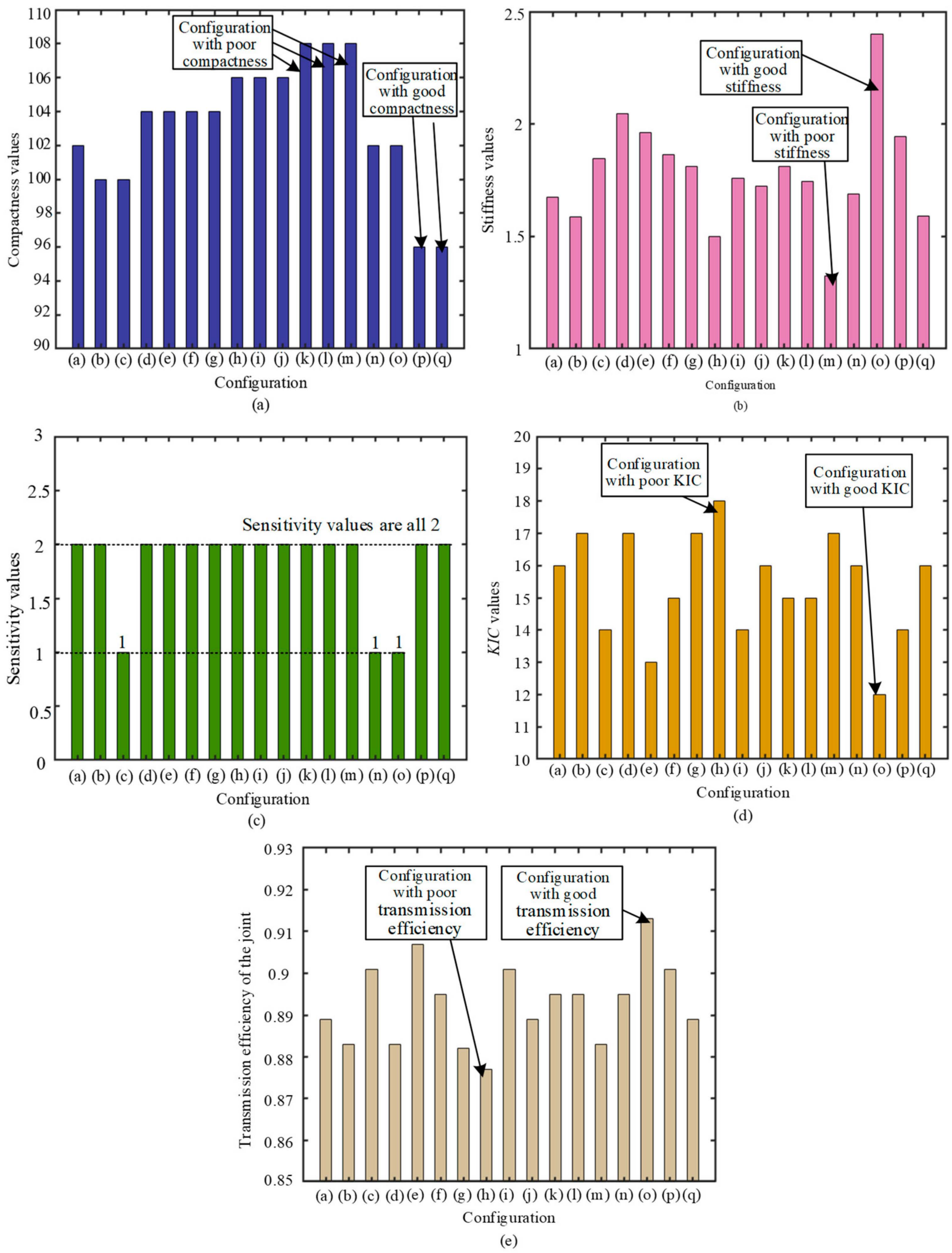

Figure 7. Values of various indicators for different configurations: (**a**) compactness values; (**b**) stiffness values; (**c**) sensitivity values; (**d**) *KIC* values; (**e**) transmission efficiency of the joint.

(3) Dynamic sensitivity. The dynamic performance of the mechanism can be evaluated through dynamic sensitivity. The dynamic sensitivity of each configuration, without considering the size and mass of the links, is determined by the minimum number of joints separating the mechanism from the frame. A lower sensitivity indicates better dynamic performance, while a higher sensitivity suggests poorer performance.

The dynamic sensitivity of the whole mechanism configuration is represented by matrix D. Any element d_i in matrix D is the minimum number of joints between each joint i and the frame. The sensitivity matrix for the configuration of Figure 6 is $D = \begin{bmatrix} 0 & 1 & 2 & 1 & 0 & 2 & 1 & 0 & 1 & 0 \end{bmatrix}$.

The dynamic sensitivity can be expressed in terms of the maximum value of the element d_{max} of matrix D. The calculated dynamic sensitivity index d_{max} for the configuration of Figure 6 is 2. Similarly, the dynamic sensitivity indices for all of the configurations in Figure 4 are presented in Figure 7c.

(4) Motion transferability. In mechanism design, it is essential to coordinate component parameters and perform kinematic analysis. For single-loop mechanisms, fewer components lead to simpler kinematic analysis. However, in multi-loop mechanisms, the number of co-loop components can vary due to different combinations of components and joint connections. A greater number of co-loop components increases the correlation between loops, generally making the kinematic analysis more complex.

Since the specific dimensions of the components are not considered at the configuration selection stage, it is not possible to quantitatively analyze the positions, velocities, and accelerations of the mechanism's components. To derive the structural characteristics of the mechanism, the topological characteristic matrix is first established. This matrix should capture information about the loops that constitute the mechanism, the types of components and joints within the loops, their connections, and their combination relationships. It is defined mathematically as shown in Equation (5).

$$LLJM = \begin{bmatrix} L_{11}/F & L_{12}/F & \ldots & L_{1m}/F \\ L_{21}/F & L_{22}/F & \ldots & L_{2m}/F \\ \ldots & \ldots & \ldots & \ldots \\ L_{l1}/F & L_{l2}/F & \ldots & L_{lm}/F \end{bmatrix} \tag{5}$$

where L_{ij} is the type of no. j component of the no. i loop, L_{ij} = ±2 for the two-joint component, and L_{ij} = ±3 for the three-parameter member. When L_{ij} is counted for the first time in the loop, the "+" sign is taken; otherwise, the "−" sign is taken. F is the number of degrees of freedom of the mechanism; the number of rows of the *LLJM* matrix, l, is the number of independent loops of the mechanism; and the number of columns of the *LLJM* matrix, m, is the maximum value of the number of components in each independent loop. Each loop is filled with the corresponding element of the *LLJM* matrix in the order of frame, input point, and output point.

In Figure 6, the mechanism has an l of 3 and an m of 6, the frame is a four-joint component, the input slider is a two-joint component, and all three output components are two-joint components, so the *LLJM* is as follows:

$$LLJM = \begin{bmatrix} 4 & 2 & 3 & 2 & 0 & 0 \\ -4 & -2 & -3 & -2 & -3 & 2 \\ -4 & -2 & -3 & -2 & 3 & 2 \end{bmatrix}$$

According to the characteristics of *LLJM*, *KIC* is used to express the structural characteristics of the mechanism, which can be represented by Equation (6).

$$KIC = \sum k_{ij} \quad \begin{cases} k_{ij} = 1 \ \text{When}\ L_{ij} \neq 0 \\ k_{ij} = 0 \ \text{When} L_{ij} = 0 \end{cases} \quad (i = 1, 2, \cdots, l;\ j = 1, 2, \cdots, m) \tag{6}$$

Informed by the analysis above, a higher number of co-loop components correlates with a greater *KIC*, indicating increased complexity in motion analysis. Conversely, efficient motion and power transmission along the mechanism's loop are preferred, with shorter transmission paths being advantageous. For the mechanism configuration depicted in Figure 6, the *KIC* is 16. Figure 7d illustrates the *KIC* for each configuration in Figure 5.

(5) Transmission efficiency of joint. During the transfer of motion and power, joints inevitably incur power loss. Consequently, the type and number of joints significantly influence the transmission performance of the kinematic chain. Once the original moving parts and the frame are established, the efficiency of each drive loop can be calculated separately to facilitate the preliminary selection of the mechanism configuration. The joint transmission efficiencies can be represented in the following matrix (Equation (7)) for the mechanism configuration.

$$\eta = \begin{bmatrix} \eta_{11} & \eta_{12} & \cdots & \eta_{1n} \\ \eta_{21} & \eta_{22} & \cdots & \eta_{2n} \\ \cdots & \cdots & \cdots & \cdots \\ \eta_{l1} & \eta_{l2} & \cdots & \eta_{ln} \end{bmatrix} \quad (7)$$

Each row in the matrix represents the transmission efficiency of each joint within its respective independent loop, progressing from the original moving part to the output member. In this context, n denotes the maximum number of joints for each independent loop; for loops containing fewer than n joints, the remaining components are filled with a value of 1.

The transmission efficiency of each independent loop can be calculated using Equation (8).

$$\eta_1 = \eta_{11}\eta_{12}\eta_{1m} \quad (8)$$

For the multi-loop mechanism with l outputs, the overall transmission efficiency of the mechanism can be calculated by averaging the transmission efficiencies of the independent branches. It can be computed as per Equation (9).

$$\eta = \frac{\eta_1 + \eta_2 + \cdots + \eta_l}{l} \quad (9)$$

Let the transmission efficiency of the translational joint be 0.97 and that of the revolute joint be 0.98. As illustrated in Figure 7e, the overall joint transmission efficiencies for each configuration in Figure 5 can be calculated accordingly.

The obtained performance indicators for each configuration are indicated in Table 4. In summary, Figure 7a illustrates that conformations (p) and (q) are more compact, while conformations (k), (l), and (m) are less so. Figure 7b indicates that configuration (o) has higher constitutive stiffness, in contrast to configuration (m), which demonstrates lower stiffness. Figure 7c shows that configurations (c), (n), and (o) possess lower sensitivity values, correlating with superior dynamic performance, whereas the other configurations exhibit higher sensitivity values and, consequently, poorer dynamic performance. Figure 7d reveals that configuration (o) has a lower KIC value, facilitating its kinematic analysis, while configuration (h) has a higher KIC value, leading to a more complex analysis. Finally, Figure 7e indicates that configuration (o) offers greater joint transmission efficiency, while configuration (g) presents lower efficiency.

Table 4. Performance metrics for multi-wing deployment mechanism configurations.

Configuration	*L*	*K*	*D*	*KIC*	η
(a)	102	1.673	2	16	0.889
(b)	100	1.587	2	17	0.883
(c)	100	1.845	1	14	0.901
(d)	104	2.045	2	17	0.883
(e)	104	1.962	2	13	0.907
(f)	104	1.864	2	15	0.895
(g)	104	1.812	2	17	0.882
(h)	106	1.5	2	18	0.877
(i)	106	1.758	2	14	0.901
(j)	106	1.725	2	16	0.889
(k)	108	1.812	2	15	0.895
(l)	108	1.745	2	15	0.895
(m)	108	1.323	2	17	0.883
(n)	102	1.689	1	16	0.895
(o)	102	2.4	1	12	0.913
(p)	96	1.943	2	14	0.901
(q)	96	1.589	2	16	0.889

3.2. Membership Function

In the comprehensive multi-indicator evaluation, the performance indicators can be categorized into three types: positive, negative, and moderate indicators. A higher value for a positive indicator signifies better performance, while a lower value for a negative indicator indicates superior performance. For moderate indicators, optimal performance is achieved when the value is closest to a predetermined target.

Among the multiple performance indicators discussed in this paper, the stiffness value and joint transmission efficiency are classified as positive indicators, while the compactness value, sensitivity value, and KIC are considered negative indicators. In the comprehensive evaluation, the indicators must be trended together at first, as outlined below:

The positivisation of the negative indicator is referenced in Equation (10).

$$x'_{ij} = 1/x_{ij} \tag{10}$$

The positivisation of the moderate indicator is derived from Equation (11).

$$x'_{ij} = 1/(x_{ij} - \mathrm{t}) \tag{11}$$

where t is the optimal value of the indicator.

Following the normalization of various evaluation indicators, it is necessary to address disparities caused by differences in scale and order of magnitude among the indicators. To achieve this, the evaluation indicators should undergo dimensionless processing. This paper employs a method that maximizes the indicators, with the membership function determined according to Equation (12).

$$Z_{ij} = x'_{ij}/\overline{x}_j \tag{12}$$

where $\overline{x}_j$ is the average of all programs for the no. j indicator.

The membership values for each indicator related to the multi-wing deployment mechanism configurations are represented in Figure 8.

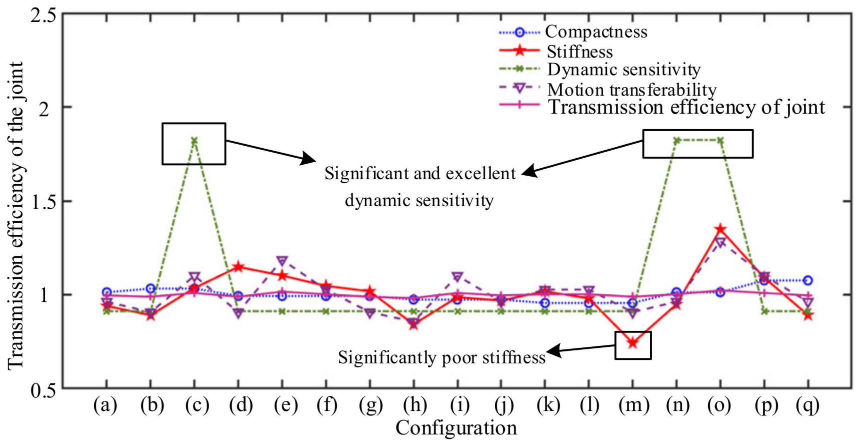

Figure 8. Membership of each indicator of multi-winged deployment mechanism configurations.

3.3. Analysis of Performance Indicators

The analytic hierarchy process (AHP) [30] is employed during the definition of indicator weights to assess the correlations between configuration performance indicators. Let a_{ij} denote the relative importance of indicator i over indicator j and a_{ji} represent the relative importance of indicator j over indicator i. If indicators i and j are equally important, both a_{ij} and a_{ji} are assigned a value of 1. If indicator i is slightly more important than indicator j, the relative importance a_{ij} is 3, while a_{ji} is 1/3. If indicator i is significantly more important than indicator j, a_{ij} is 5, and a_{ji} is 1/5. If indicator i is strongly more important than indicator j, a_{ij} is 7, and a_{ji} is 1/7. The resulting table of relative importance is shown in

Table 5. Given the varying importance of each indicator to the mechanism's performance, hierarchical analysis is used to establish the weight coefficients for each indicator, resulting in the correlations presented in Table 5.

Table 5. Configuration performance indicator correlations.

	L	***K***	***D***	***KIC***	$\boldsymbol{\eta}$
L	1	1/3	1/3	1/3	1/3
K	3	1	1/3	1/3	1/3
D	3	3	1	1/3	1/3
KIC	3	3	3	1	1/3
η	3	3	3	3	1

Then, the judgment matrix A is as follows:

$$A = \begin{bmatrix} 1 & 1/3 & 1/3 & 1/3 & 1/3 \\ 3 & 1/3 & 1/3 & 1/3 & 1/3 \\ 3 & 3 & 1 & 1/3 & 1/3 \\ 3 & 3 & 3 & 1 & 1/3 \\ 3 & 3 & 3 & 3 & 1 \end{bmatrix}$$

Due to the inherent subjectivity of the judgment matrix, the root method is employed to determine the eigenvector of the matrix.

The initial weighting coefficients are calculated according to Equation (13).

$$W_i' = \sqrt[m]{a_{i1}a_{i2}\cdots a_{im}} \tag{13}$$

where i is the no. i indicator; m is the total number of indicators; and a is the value of the indicator correlation.

The normalized weighting coefficients W_i are calculated as indicated in Equation (14).

$$W_i = W_i' / \sum_{i=1}^{m} W_i' \tag{14}$$

The weights of each indicator are calculated utilizing Equations (13) and (14), as illustrated in Figure 9.

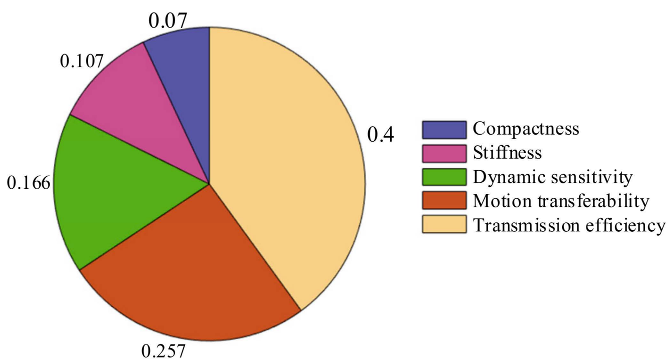

Figure 9. Normalization indicator weights for each configuration.

3.4. Fuzzy Comprehensive Evaluation

The weighted average operator is employed to conduct a comprehensive evaluation of all relevant factors. This approach establishes a fuzzy comprehensive evaluation model specifically for the configuration of the multi-wing deployment mechanism. The model is represented in Equation (15).

$$b_j = \sum_{i=1}^{m} \left(a_i r_{ij}\right) \quad (\mathrm{j} = 1, 2, \cdots, \mathrm{n}) \tag{15}$$

where i is the no. i indicator, j is the no. j scheme, m is the total number of indicators, n is the total number of schemes, a is the weight of the indicator, and r is the degree of membership.

From Figure 8, the weight matrix is as follows:

$$A = \begin{bmatrix} 0.07 & 0.107 & 0.166 & 0.257 & 0.4 \end{bmatrix}$$

From Figure 8, the evaluation matrix is as follows:

$$R_{5\times17} = \begin{bmatrix} 1.013 & 1.033 & 1.033 & \cdots & 1.013 & 1.013 & 1.076 & 1.076 \\ 0.94 & 0.891 & 1.036 & \cdots & 0.949 & 1.348 & 1.091 & 0.892 \\ 0.912 & 0.912 & 1.824 & \cdots & 1.824 & 1.824 & 0.912 & 0.912 \\ 0.963 & 0.907 & 1.101 & \cdots & 0.963 & 1.284 & 1.101 & 0.963 \\ 0.996 & 0.989 & 1.009 & \cdots & 1.002 & 1.023 & 1.009 & 0.996 \end{bmatrix}$$

In the comprehensive evaluation and optimization process, the comprehensive evaluation result matrix B is obtained by multiplying the weight matrix with the evaluation matrix R of each indicator.

$$B = A{\cdot}R = \begin{bmatrix} 0.969 & 0.948 & 1.173 & \cdots & 1.124 & 1.257 & 1.030 & 0.968 \end{bmatrix}$$

The results are ranked by drawing on the comprehensive evaluation outcomes, as detailed in Figure 10.

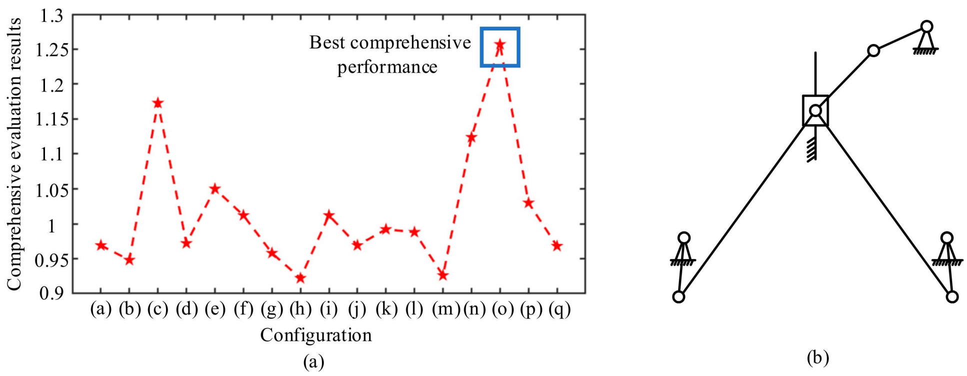

Figure 10. Comprehensive evaluation results of each multi-wing deployment mechanism configuration: (**a**) comprehensive evaluation value of each configuration; (**b**) optimal configuration.

According to the principle of maximizing membership degree, configuration (o) demonstrates superior overall performance, followed by configuration (c), while configuration (h) exhibits relatively poor performance.

4. Design and Functional Verification

The configurations obtained from the comprehensive evaluation demonstrate superior performance. This section performs performance calculations on multiple mechanisms derived from the configuration evolution, thereby validating the rationality of the selected configurations. Furthermore, simulations and experiments are conducted to verify the functional feasibility of synchronous deployment of multiple wings under a single drive.

4.1. Performance Comparison Analysis

To ensure the synchronized deployment of the three sets of folding wings, the mechanism must enable the rotation of three cranks—each connected to a folding wing—by a specific angle using a single driving source. This requires calculating the mechanism's dimensions to meet motion requirements and analyzing its transmission efficiency. The initial folded and deployed states, along with the vector models of the selected three configurations, are detailed in Table 6.

Table 6. Folding and unfolding states and vector models of the three configurations.

Configuration	Folding State	Deployable State	Vector Model
(o)	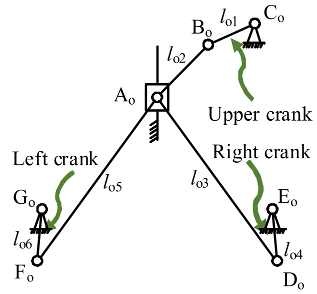	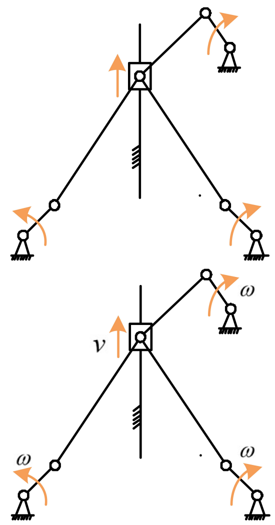	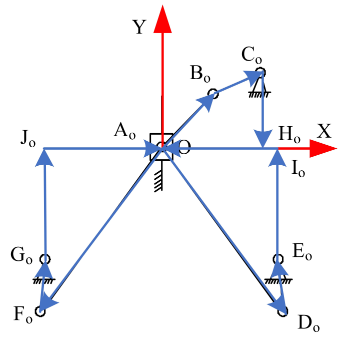
(c)	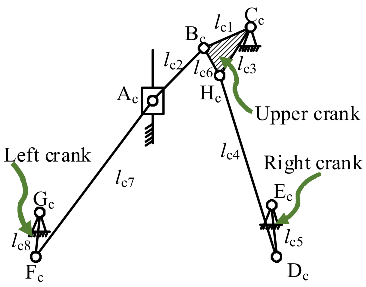	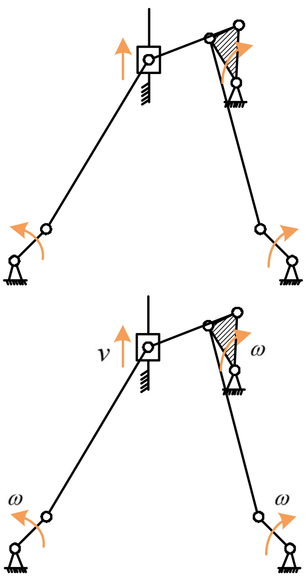	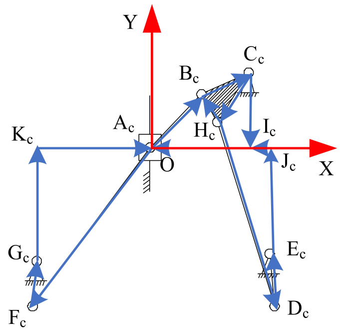

Table 6. *Cont.*

Configuration	Folding State	Deployable State	Vector Model
(e)	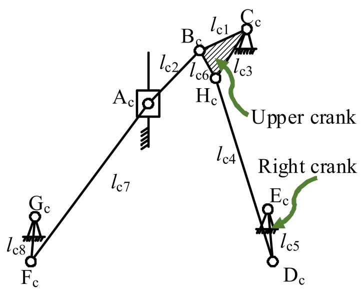	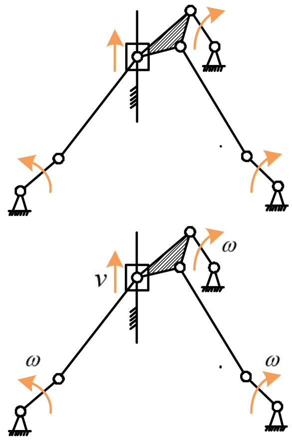	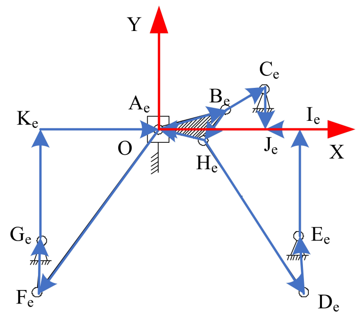

Informed by the relationships between the components in the vector model coordinate system, the vector constraint relationships for each configuration are established. The closed-loop vector equations for configuration (o) are detailed in Equation (16).

$$\begin{cases} \overrightarrow{A_oB_o} + \overrightarrow{B_oC_o} + \overrightarrow{C_oH_o} + \overrightarrow{H_oA_o} = \overrightarrow{0} \\ \overrightarrow{A_oD_o} + \overrightarrow{D_oE_o} + \overrightarrow{E_oI_o} + \overrightarrow{I_oA_o} = \overrightarrow{0} \\ \overrightarrow{A_oF_o} + \overrightarrow{F_oG_o} + \overrightarrow{G_oJ_o} + \overrightarrow{J_oA_o} = \overrightarrow{0} \end{cases} \tag{16}$$

The closed-loop vector equations for configuration (c) are presented in Equation (17).

$$\begin{cases} \overrightarrow{A_cB_c} + \overrightarrow{B_cC_c} + \overrightarrow{C_cJ_c} + \overrightarrow{J_cA_c} = \overrightarrow{0} \\ \overrightarrow{B_cC_c} + \overrightarrow{C_cH_c} + \overrightarrow{H_cB_c} = \overrightarrow{0} \\ \overrightarrow{C_cH_c} + \overrightarrow{H_cD_c} + \overrightarrow{D_cE_c} + \overrightarrow{E_cI_c} + \overrightarrow{I_cC_c} = \overrightarrow{0} \\ \overrightarrow{A_cF_c} + \overrightarrow{F_cG_c} + \overrightarrow{G_cK_c} + \overrightarrow{K_{cC}A_c} = \overrightarrow{0} \end{cases} \tag{17}$$

The closed-loop vector equations corresponding to configuration (e) are provided in Equation (18).

$$\begin{cases} \overrightarrow{A_eB_e} + \overrightarrow{B_eC_e} + \overrightarrow{C_eJ_e} + \overrightarrow{J_eA_e} = \overrightarrow{0} \\ \overrightarrow{A_eB_e} + \overrightarrow{B_eH_e} + \overrightarrow{H_eA_e} = \overrightarrow{0} \\ \overrightarrow{C_eB_e} + \overrightarrow{B_eH_e} + \overrightarrow{H_eD_e} + \overrightarrow{D_eE_e} + \overrightarrow{E_eI_e} + \overrightarrow{I_eC_e} = \overrightarrow{0} \\ \overrightarrow{A_eF_e} + \overrightarrow{F_eG_e} + \overrightarrow{G_eK_e} + \overrightarrow{K_eA_e} = \overrightarrow{0} \end{cases} \tag{18}$$

From the vector equations of each configuration, it can be observed that the motion of configuration (o) is relatively simple, making its dimensional calculations easier. In contrast, the motions of configurations (c) and (e) are more complex, resulting in more challenging dimensional calculations. Leveraging the motion requirements of the mechanism and certain spatial constraints, 10 different sets of dimensional parameters are calculated for configuration O, labeled O1 to O10. Similarly, 10 sets of parameters are calculated for configurations (c) and (e), labeled C1 to C10 and E1 to E10, respectively. The transmission efficiency for each set is computed, and the results are shown in Figure 11.

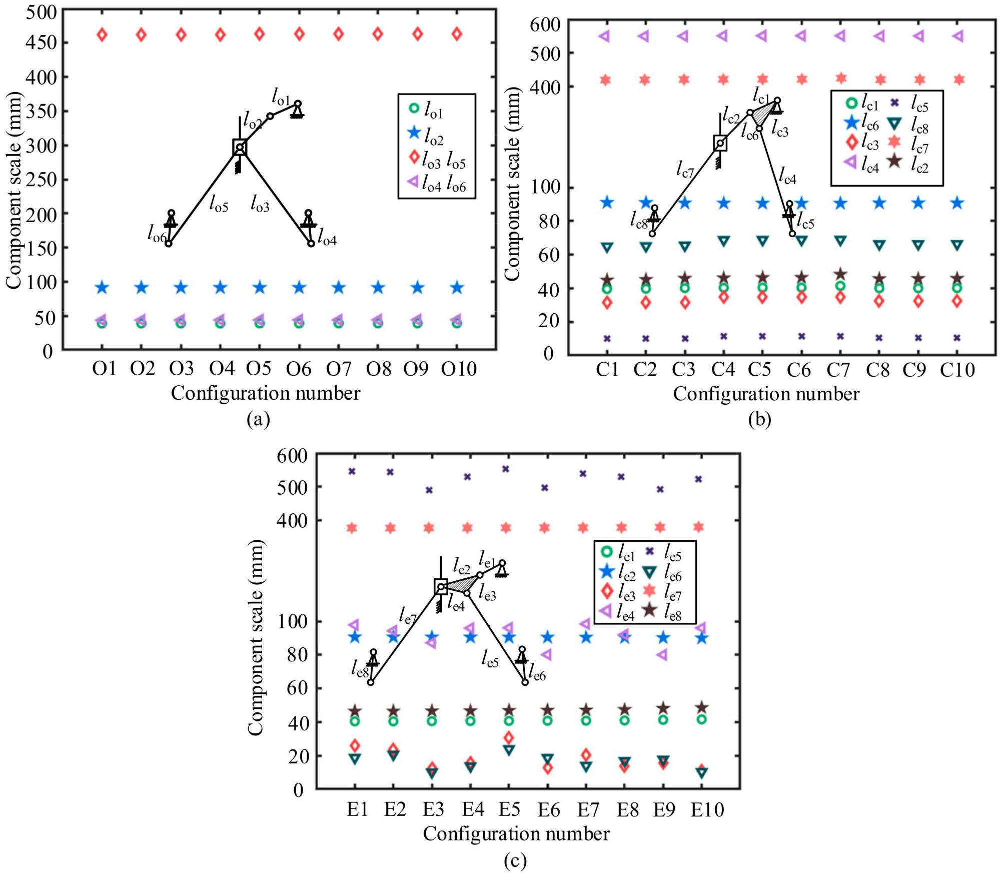

Figure 11. Scale information of each configuration: (**a**) dimensional parameters of configuration (o); (**b**) dimensional parameters of configuration (c); (**c**) dimensional parameters of configuration (e).

The transmission efficiency for each configuration under various dimensional parameters is presented in Figure 12. The results indicate that the transmission efficiency of configuration (o) consistently exceeds that of configurations (c) and (e).

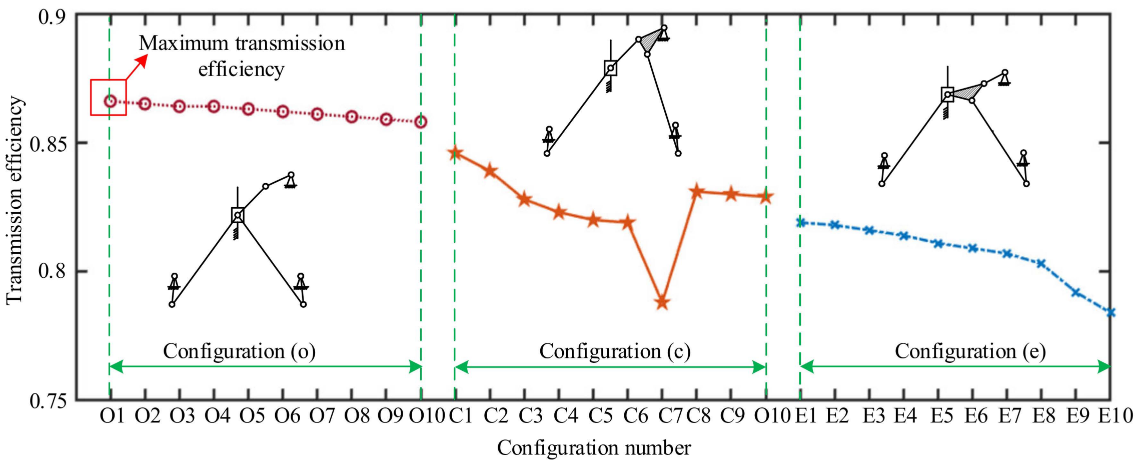

Figure 12. Comparison of transmission efficiency across different configurations and dimensions.

Configuration (o) corresponds to mechanism O1, which exhibits the maximum transmission efficiency, while O10 demonstrates the minimum efficiency. For configuration (c), mechanism C1 achieves the highest transmission efficiency, whereas C7 shows the lowest.

In configuration (e), mechanism E1 has the maximum transmission efficiency, and E10 has the minimum. Detailed parameters are provided in Table 7.

Table 7. Dimensional parameters and transmission efficiency of configuration (c).

No.	O1 (max)	O10 (min)	C1 (max)	C7 (min)	E1 (max)	E10 (min)
η	0.866	0.858	0.846	0.788	0.819	0.784

Configuration (o) achieves a maximum transmission efficiency of 0.866 across ten different scale parameters, with a minimum of 0.858. In comparison, configuration (c) reaches a maximum efficiency of 0.846, while configuration (e) achieves a maximum of 0.819. Notably, the highest transmission efficiency for configuration (o) is 2.4% greater than that of configuration (c) and 5.7% higher than that of configuration (e). These results demonstrate that the optimized configuration meets practical requirements. Moreover, the performance indicators proposed in this study can be generalized and applied to the optimization of other mechanism designs.

4.2. Functional Verification

According to the comprehensive evaluation results of the multi-wing deployment mechanism configuration, configuration (o) is further developed, resulting in the multi-wing deployment mechanism presented in Figure 13. The drive source propels the slider upward along the upper rail, causing the upper, left, and right connecting links to move accordingly. This movement, in turn, drives the upper, left, and right cranks to rotate around the frame, enabling the corresponding folding wings attached to each crank to rotate and unfold.

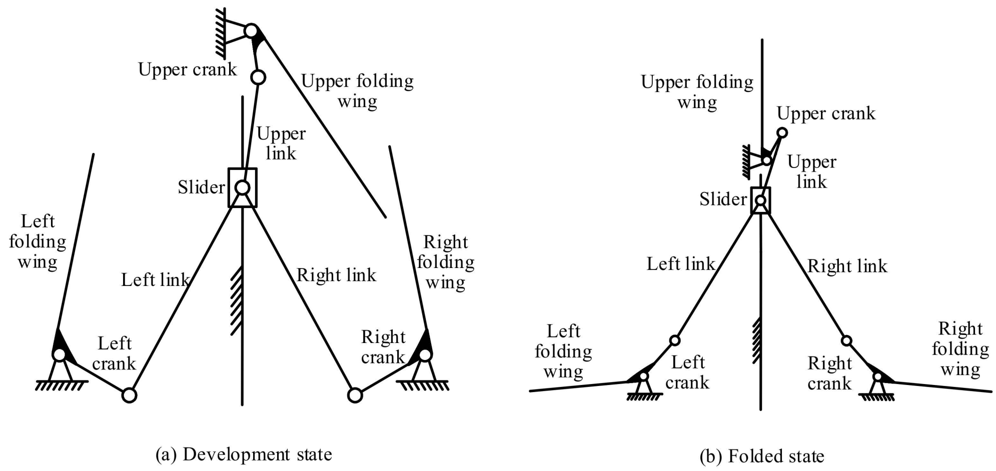

Figure 13. Sketch of the multi-wing deployment mechanism.

To verify the functional feasibility of the designed mechanism, a kinematic simulation analysis is conducted on the multi-wing unfolding mechanism using ADAMS, as depicted in Figure 14. The simulation model depicts how the slider applies an upward driving force to facilitate the unfolding of three sets of folding wings. The motion process of the single-drive, three-folding-wings deployable mechanism is shown in Figure 15. The resulting angular displacements for each wing during the unfolding process are shown in Figure 16.

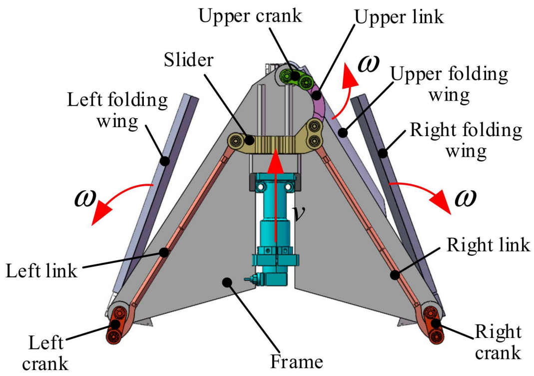

Figure 14. Simulation model of multi-wing deployment mechanism.

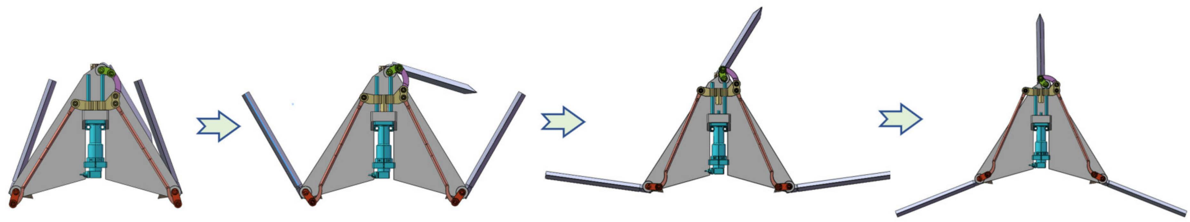

Figure 15. The motion process of the single-drive, three-wing deployable mechanism.

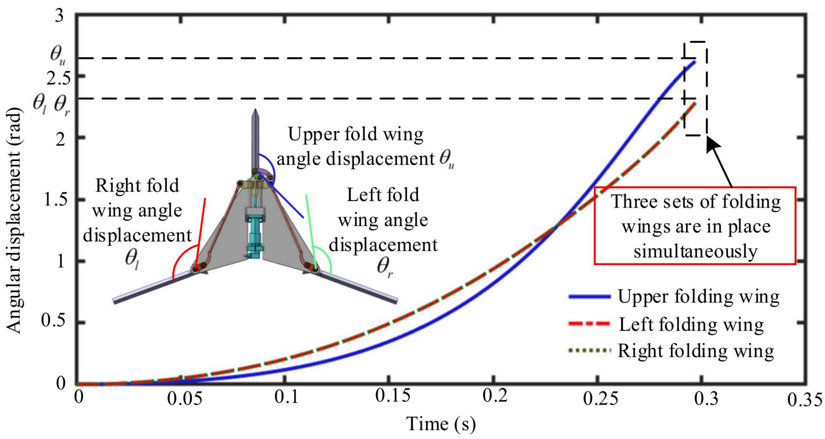

Figure 16. Kinematic simulation results.

The kinematic simulation indicates that the three sets of folding wings can be unfolded simultaneously at different angles using the same slider drive. Therefore, the designed multi-wing unfolding mechanism is deemed feasible.

As detailed in Figure 17, a prototype of the multi-wing deployment mechanism was fabricated and assembled, informed by the designed parameters, followed by experimental testing. The multi-wing deployment mechanism is made of an aluminum alloy, and the folding wing control surface is made of 3D-printed resin. The multi-wing deployment mechanism is fixed onto the experimental platform. An electric push cylinder serves as the drive source to move the slider upward, thereby facilitating the unfolding of the wings. Targets are attached to the crank connected to the folded wing, and a high-speed camera captures the motion information of the targets, transmitting the data to the data acquisition system. To ensure optimal performance of the high-speed camera, a lighting fixture is arranged to enhance the illumination. The measured changes in the angular displacement of each unfolding wing are presented in Figure 18.

Figure 17. Experimental test of multi-wing deployment mechanism.

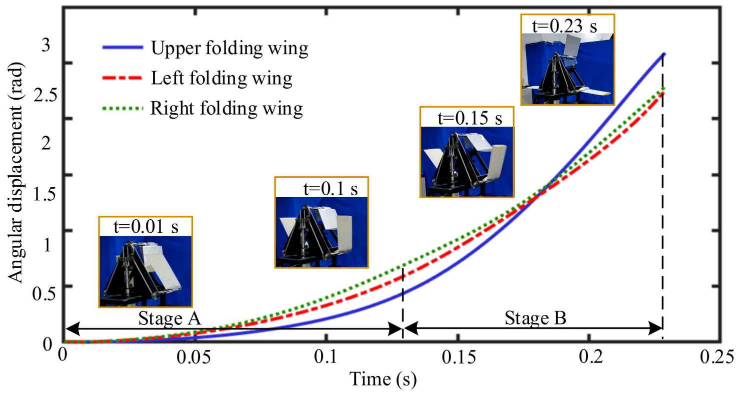

Figure 18. Experimental results.

The experimental data in Figure 18 demonstrate that the multi-wing deployment mechanism can unfold rapidly in under one second. Additionally, the folding wings operate without interference during the unfolding process, enabling different wings to rotate at varying angles under the same driving force. Although there is a slight discrepancy in the displacement of the left and right folding wings compared to the ideal state, this can be attributed to gaps present during the prototype assembly. Consequently, the multi-wing deployment mechanism designed in this study is deemed feasible.

5. Conclusions

This paper proposes a design method for a multi-wing deployment mechanism based on multiple performance indicators and configuration topology, enabling the synchronous deployment of multiple folding wings from a single drive. Initially, a specific topology for an eight-link mechanism is developed to meet the functional requirements of the multi-wing deployment mechanism, resulting in seventeen distinct configurations. Secondly, a quantitative expression method is introduced for performance indicators, including compactness, stiffness, dynamic sensitivity, motion transmission, and joint transmission efficiency within these configurations. The optimal multi-wing deployment mechanism is then identified using a fuzzy comprehensive evaluation. Additionally, the transmission efficiency of various configurations is calculated across different scales. Finally, the feasibility of the designed mechanism is validated through simulation and experimental testing, providing a new design method for the development of folding wing deployment mechanisms in aircraft. The optimized configuration consistently exhibited higher transmission efficiencies compared to the other configurations, with maximum efficiencies exceeding those of other configurations by 2.4% and 5.7%. This result demonstrates the effectiveness of the proposed optimization design method.

This study presents a new approach to mechanism design by incorporating performance indicators during the configuration stage, thereby facilitating the optimization of configurations with respect to performance. In the future, it is possible to further integrate scale effects into this framework, establishing a comprehensive design system that unifies configuration, scale, and performance.

Author Contributions: Conceptualization, G.Z.; methodology, G.Z.; software, G.Z.; validation, G.Z.; formal analysis, G.Z.; investigation, G.Z.; resources, G.Z.; data curation, G.Z.; writing—original draft preparation, G.Z.; writing—review and editing, G.Z., G.Y., R.Z. and C.Y.; visualization, G.Z.; supervision, J.T. and H.G.; project administration, R.L.; funding acquisition, H.X., H.G., G.Y. and R.L. All authors have read and agreed to the published version of the manuscript.

Funding: This research has received grants from the National Natural Science Foundation of China (NSFC) through grants nos. 52192634, 52105013, 52405013, and U2341237 and the China Postdoctoral Science Foundation (no. 2023T160168).

Institutional Review Board Statement: Not applicable.

Informed Consent Statement: Not applicable.

Data Availability Statement: The original contributions presented in the study are included in the article, further inquiries can be directed to the corresponding author.

Conflicts of Interest: The authors declared no potential conflicts of interest with respect to the research, authorship, and publication of this article.

References

1. Jia, H.; Zheng, H.; Zhou, H.; Zhang, Q. Aerodynamic optimization and characterization of a ducted tail for a box-launched aircraft. *Appl. Sci.* **2024**, *14*, 6496. [CrossRef]
2. Zhang, X.; Cheng, G.; Chen, G. A New Type Bionic Foldable Wing Design for High Maneuverable Unmanned Aerial Vehicle. *Appl. Sci.* **2023**, *13*, 8345. [CrossRef]
3. Demircali, A.A.; Huseyin, U. Mini glider design and implementation with wing-folding mechanism. *Appl. Sci.* **2018**, *8*, 1541. [CrossRef]
4. Ni, Y.; Zhang, W.; Lv, Y. Multi-body dynamics modeling and transient characteristics analysis for a folding wing. *Rev. Int. Métodos Numéricos Cálculoy Diseñoen Ing.* **2020**, *37*, 1–19. [CrossRef]
5. Yun, Z.; Feng, Y.; Tang, X.; Chen, L. Analysis of motion characteristics of bionic morphing wing based on Sarrus linkages. *Appl. Sci.* **2022**, *12*, 6023. [CrossRef]
6. Zhang, S.Y.; Tang, J.L.; Ren, H. Analysis of mechanical deployment system for combustion-gas-actuated folded wings. *J. Solid Rocket Technol.* **2010**, *33*, 481–485.
7. Zhao, J.F. Dynamic simulation and optimization design of folding wing deployment. *J. Proj. Rockets Missiles Guid.* **2012**, *32*, 155–157.
8. Ybarra, M. Air force suspends spending on parts of ALCM program. *Inside Missile Def.* **2011**, *17*, 7–8.
9. Sun, L.; Cui, R.; Yang, W.; Ye, Z.; Zhou, Y.; Wu, C. Automatic synthesis of the complete set of contracted graphs for planar kinematic chains with up to seven independent loops. *Mech. Mach. Theory* **2021**, *156*, 104144. [CrossRef]
10. Deng, T.; Xu, H.; Tang, P.; Liu, P.; Yan, L. A novel algorithm for the isomorphism detection of various kinematic chains using topological index. *Mech. Mach. Theory* **2020**, *146*, 103740. [CrossRef]
11. Amine, S.; Prasad, B.; Saber, A.; Mokhiamar, O.; Gazo-Hanna, E. Design and Analysis of a Planar Six-Bar Crank-Driven Leg Mechanism for Walking Robots. *Appl. Sci.* **2024**, *14*, 8919. [CrossRef]
12. Yang, F.; Deng, Z.; Tao, J.; Li, L. A new method for isomorphism identification in topological graphs using incident matrices. *Mech. Mach. Theory* **2012**, *49*, 298–307. [CrossRef]
13. He, L.; Liu, F.; Sun, L.; Wu, C. Isomorphic identification for kinematic chains using variable high-order adjacency link values. *J. Mech. Sci. Technol.* **2019**, *33*, 4899–4907. [CrossRef]
14. Sun, L.; Ye, Z.; Cui, R. Compound topological invariant based method for detecting isomorphism in planar kinematic chains. *J. Mech. Robot.* **2020**, *12*, 054504. [CrossRef]
15. Wang, Y.; Cui, R.; Chen, J. A novel compound topological invariant for isomorphism detection of planar kinematic chains. *Mech. Sci.* **2022**, *13*, 585–591. [CrossRef]
16. Nie, S.; Liao, A.; Qiu, A.; Gong, S. Addition method with 2 links and 3 pairs of type synthesis to planar closed kinematic chains. *Mech. Mach. Theory* **2012**, *58*, 179–191. [CrossRef]

17. Dobrjanskyj, L.; Freudenstein, F. On a Theory for the Type Synthesis of Mechanisms. In Proceedings of the 11th International Congress of Applied Mechanics, Munich, Germany, 30 August–5 September 1964; Springer: Berlin, Germany, 1964; pp. 420–428.
18. Ding, H.; Hou, F.; Kecskeméthy, A.; Huang, Z. Synthesis of the whole family of planar 1-DOF kinematic chains and creation of their atlas database. *Mech. Mach. Theory* **2012**, *47*, 1–15. [CrossRef]
19. Xu, L.; Chen, Q.; He, L.; Li, Q. Kinematic analysis and performance evaluation of a redundantly actuated hybrid manipulator. In Proceedings of the Intelligent Robotics and Applications, Wuhan, China, 16–18 August 2017; Volume 10463.
20. Sancibrian, R.; Viadero, F.; Garcıa, P.; Fernández, A. Gradient-based optimization of path synthesis problems in planar mechanisms. *Mech. Mach. Theory* **2004**, *39*, 839–856. [CrossRef]
21. Acharyya, S.K.; Mandal, M. Performance of EAs for four-bar linkage synthesis. *Mech. Mach. Theory* **2009**, *44*, 1784–1794. [CrossRef]
22. Peñuñuri, F.; Peón-Escalante, R.; Villanueva, C.; Pech-Oy, D. Synthesis of mechanisms for single and hybrid tasks using differential evolution. *Mech. Mach. Theory* **2011**, *46*, 1335–1349. [CrossRef]
23. El-Shakery, S.; Rokaya, R.; Khaled, K. Analytical and Graphical Optimal Synthesis of Crank-Rocker Four Bar Mechanisms for Achieving Targeted Transmission Angle Deviations. *Jordan J. Mech. Ind. Eng.* **2020**, *14*, 303–313.
24. Yoon, G.; Jae, C. Constraint force design method for topology optimization of planar rigid-body mechanisms. *Comput.-Aided Des.* **2012**, *44*, 1277–1296. [CrossRef]
25. Liu, X.; Ding, J.; Wang, C. Design framework for motion generation of planar four-bar linkage considering clearance joints and dynamics performance. *Machines* **2022**, *10*, 136. [CrossRef]
26. Han, S.; Yoon, Y. Topology optimization of linkage mechanisms simultaneously considering both kinematic and compliance characteristics. *J. Mech. Des.* **2021**, *143*, 061704. [CrossRef]
27. Wang, R.; Huang, F.; Huang, H.; Chen, J. Configuration synthesis and screening method for multiple closed-loop unit tandem mechanisms. *Mech. Mach. Theory* **2024**, *202*, 105770. [CrossRef]
28. Shin, J.K.; Krishnamurty, S. Standard code technique in the enumeration of epicyclic geartrains. *Mech. Mach. Theory* **1993**, *28*, 347–355. [CrossRef]
29. Wang, H.; Huang, Q.; Li, C. *Graph Theory Algorithm and Its MATLAB Implementation*; Beihang University Press: Beijing, China, 2010; pp. 21–25.
30. Chernukhin, R.V.; Dronov, A.A.; Blashchuk, M.Y. The application of the analytic hierarchy process when choosing layout schemes for a geokhod pumping station. *Mater. Sci. Eng.* **2015**, *91*, 012086. [CrossRef]